remote sensing

MDPI

Article

A Systematic Classification Method for Grassland Community Division Using China's ZY1-02D Hyperspectral Observations

Dandan Wei [1], Kai Liu [1,2], Chenchao Xiao [1], Weiwei Sun [2,*], Weiwei Liu [2], Lidong Liu [2], Xizhi Huang [1,3] and Chunyong Feng [1,3]

[1] Land Satellite Remote Sensing Application Center, Ministry of Natural Resources, Beijing 100048, China
[2] Department of Geography and Spatial Information Techniques, Ningbo University, Ningbo 315211, China
[3] Faculty of Geographical Science, Beijing Normal University, Beijing 100875, China
* Correspondence: sunweiwei@nbu.edu.cn

Abstract: The main feature of grassland degradation is the change in the vegetation community structure. Hyperspectral-based grassland community identification is the basis and a prerequisite for large-area high-precision grassland degradation monitoring and management. To obtain the distribution pattern of grassland communities in Xilinhot, Inner Mongolia Autonomous Region, China, we propose a systematic classification method (SCM) for hyperspectral grassland community identification using China's ZiYuan 1-02D (ZY1-02D) satellite. First, the sample label data were selected from the field-collected samples, vegetation map data, and function zoning data for the Nature Reserve. Second, the spatial features of the images were extracted using extended morphological profiles (EMPs) based on the reduced dimensionality of principal component analysis (PCA). Then, they were input into the random forest (RF) classifier to obtain the preclassification results for grassland communities. Finally, to reduce the influence of salt-and-pepper noise, the label similarity probability filter (LSPF) method was used for postclassification processing, and the RF was again used to obtain the final classification results. The results showed that, compared with the other seven (e.g., SVM, RF, 3D-CNN) methods, the SCM obtained the optimal classification results with an overall classification accuracy (OCA) of 94.56%. In addition, the mapping results of the SCM showed its ability to accurately identify various ground objects in large-scale grassland community scenes.

Keywords: grassland communities; hyperspectral remote sensing; ZY1-02D satellite; systematic classification method

Citation: Wei, D.; Liu, K.; Xiao, C.; Sun, W.; Liu, W.; Liu, L.; Huang, X.; Feng, C. A Systematic Classification Method for Grassland Community Division Using China's ZY1-02D Hyperspectral Observations. *Remote Sens.* **2022**, *14*, 3751. https://doi.org/10.3390/rs14153751

Academic Editors: Bingfang Wu, Yuan Zeng and Dan Zhao

Received: 13 July 2022
Accepted: 3 August 2022
Published: 5 August 2022

1. Introduction

Grasslands are one of the most widely distributed vegetation types in the world. They cover nearly 25% of the land area and are an important component of terrestrial ecosystems [1,2]. In addition, they provide an important food supply for ruminant milk and meat production, and store approximately 20% of the global carbon stock, thus playing a key role in balancing greenhouse gas concentrations [2–4]. China is one of the richest countries in the world in terms of grass resources, with a total grassland area of approximately 400 million ha, accounting for approximately 40% of the country's total land area [2]. Grassland vegetation dominates China's green ecological barrier from the northeastern plains through the Inner Mongolia Plateau and Loess Plateau to the Xinjiang Mountains and the Qinghai-Tibet Plateau [5]. However, due to the effects of climate change (e.g., warming) and human activities (e.g., population growth and overgrazing), grassland areas worldwide have been degraded. The result leads to a decrease in water storage capacity and severe soil erosion, further leading to natural disasters such as rodent infestation and dust storms and floods, which directly affect sustainable socioeconomic development [6,7]. As a result, grassland degradation monitoring is particularly important [8,9]. The basis and prerequisite of grassland degradation monitoring is the monitoring of grassland

communities, and monitoring should include the reduction in grassland cover, the change in grassland community structure, and changes in species. Therefore, the monitoring of grassland communities and identifying the degradation indicator species in grassland communities are important links between grassland degradation process monitoring and grassland ecological restoration management.

A biological community is a collection of various biological populations living in a specific area or habitat [10]. It consists of certain species, has a certain appearance and structure, has a certain distribution range, and has other basic characteristics. Among them, species composition of the community is the most important factor used to determine the nature of the community and is the basic characteristic used to identify different community types [11,12]. Traditional grassland community monitoring mainly relies on manual fieldwork, and the results mainly depend on the professional level and practical experience of the detectors. This method results in low accuracy, and it is extremely difficult to obtain regional data in real time and on a large scale due to the extremely wide distribution of grassland communities. Additionally, this method consumes many human and material resources, thus restricting the effective promotion of grassland ecological restoration [5,13,14]. With the development of science and technology, the monitoring of grasslands is gradually improving, with trends indicating higher efficiency, higher accuracy, and larger spatial scales [15].

After nearly 60 years of development, remote sensing technology is widely used in the fields of earth resources, environmental science, and disaster monitoring, as remote sensing data acquired for large spatial scales compensate for the spatial limitations of traditional ground-based survey methods [16–19]. The sensors carried in satellites can acquire visible near-infrared, shortwave infrared, microwave, and other electromagnetic wavelength bands, and remote sensing images such as panchromatic, multispectral [20,21], hyperspectral [22], and synthetic aperture radar (SAR) have been developed [23,24]. Panchromatic and multispectral images contain only one or more wavebands with information expressiveness; additionally, SAR images require complex preprocessing steps and considerable specialized basic knowledge. In contrast, hyperspectral images (HSIs), as the current forefront in the field of remote sensing technology, contain rich information regarding space, radiation, and spectra [25,26]. In addition, due to the high similarity between different grassland communities, it is common for the same species to have different spectra and for different species to have the same spectrum, which makes identification difficult [27]. Therefore, the use of HSIs has become the first choice for high-precision ground object identification and classification research.

Supervised classification is the process of using the image elements of the identified category to identify the image elements of other categories [28,29]. Before classification, we have a priori knowledge of the feature classes of certain sample areas on the image based on visual interpretation and field surveys. Then, we select certain training samples and train the model using the judgment function to classify each image element to its most similar sample class according to different rules to complete the classification of the whole image, e.g., support vector machine (SVM) [30], random forest (RF) [21], and spectral angle mapper (SAM) [31]. However, most of these methods focus only on spectral information, making it difficult to accurately classify complex objects. In recent years, many scholars have successively proposed a variety of classification methods based on spatial-spectral feature extraction. These methods are dedicated to extracting spatial-spectral features with high recognition rates to further improve the classification accuracy. Camps-Valls et al. [32] combined spatial and spectral information to construct a family of composite kernels and presented a classification framework of support vector machine with composite kernels (SVM-CK). Li et al. [33] constructed a training sample-based collaborative dictionary and incorporated contextual regression pixels to build a collaborative representation-based classification (CRC) process. Gao et al. [34] presented a multiscale conservative smoothing algorithm to reduce noise and extract the spatial structure from coarse levels to fine levels and then implemented the adaptive sparse representation classifier on integrated spatial-spectral characteristics of the HSIs. Moreover, spatial information can be used to

regularize previously obtained classification maps from regular classifiers. For example, Cao et al. [35] implemented the cascaded Markov random field (MRF) to concatenate the contextual information with the predicted probability of the SVM and achieved the final promoted classification map. Kang et al. [36]. used the guiding images that reflect the homogeneity disruption to improve the edge-preserving performance of classification maps from a preliminary SVM classifier. Deep learning surpasses the accuracy of traditional classification methods due to its powerful feature extraction capabilities and end-to-end training approach. Xu et al. [37] proposed a deep feature fusion network structure based on residual learning, and this structure can be used to obtain better classification results. In addition, the spectral-spatial fully convolutional network conditional random field (SSFCN-CRF) [38] is a pixel-based classification method that uses two weighting factors to distinguish the importance of spatial-spectral features. In addition, the attention-based adaptive spectral–spatial kernel improved residual network (A^2S^2K-ResNet) [39] is an adaptive spatial-spectral kernel improved residual network based on the attention mechanism, which can capture spatial-spectral characteristics by combining the attention mechanism.

Although these feature extraction-based classification methods have improved classification accuracy to some extent, there are still some problems that must be addressed. Feature extraction methods based on deep learning generally require a large number of samples to train the deep network, while the number of training samples in the classification process of HSIs is generally small. This method fundamentally limits the classification effect, makes interpretability more difficult, and requires the use of more human and material resources to tune the parameters, thus limiting its application in practical production [40]. In addition, the grassland community has a complex structure and low vegetation, and the model based on manual feature extraction does not fully consider the systematic approach of classification, including feature extraction before classification and processing after classification, and this lack of consideration limits the classification accuracy to some extent.

To solve the above problems, this paper proposes a systematic classification method (SCM) for grassland communities, including sample selection, preclassification processing, feature-based classification, and postclassification processing. First, based on the field collected samples, updated vegetation map (1:1,000,000) data (hereafter referred to as vegetation map data) and function zoning data for the Nature Reserve (hereafter referred to as function zoning data), some pixels within the study area were selected as the sample label data. Second, the features of the HSIs of grassland communities were obtained using extended morphological profiles (EMPs) [41]. Then, the extracted features were combined with the sample label data, and preclassification results were obtained using random forest (RF). Finally, the classification results were postprocessed using the label similarity probability filter (LSPF) method, and further classification was performed using RF to reduce the influence of salt-and-pepper noise on the classification results. This method can effectively remedy the problems of poor classification performance and low accuracy of traditional classification methods and provides a complete classification process for grassland community identification.

The rest of this paper is organized as follows. Section 2 presents the experimental data, study area, and auxiliary data for grassland community classification. A systematic classification method for grassland community division is proposed in Section 3. Section 4 evaluates and discusses the performance of the proposed method on hyperspectral datasets. Section 5 is the summary.

2. Materials

2.1. Experimental Data

2.1.1. ZY1-02D Hyperspectral Data and Preprocessing

The ZiYuan 1-02D (ZY1-02D) satellite (5-m optical satellite) is a medium-resolution earth observation satellite launched on 12 September 2019, to serve broadband observation and quantitative remote sensing missions [28,42]. The satellite is mainly equipped with two payloads: a visible and near-infrared camera (VNIC) and an advanced hyperspectral

imager (AHSI). The AHSI, ranging from 0.4 to 2.5 μm, has 166 spectral bands, including 76 spectral bands in visible near-infrared (VNIR) and 90 spectral bands in shortwave infrared (SWIR) [43,44]. The satellite orbits in a sun-synchronous orbit of 778 km, and the revisiting cycle can be as short as three days. Table 1 lists the information of the AHSI sensor in ZY1-02D. The HSIs from ZY1-02D can provide data for large-scale natural resource surveys and monitoring.

Table 1. ZY1-02D satellite payloads information.

Satellite Payloads	**ZY-1-02D**
Launch Country	China
Launch Time	12 September 2019
Number of Bands	76 (VNIR), 90 (SWIR)
Spectral Range (nm)	400–2500
Spectral Resolution (nm)	10 (VNIR), 20 (SWIR)
Spatial Resolution (m)	30
Swath Width (km)	60

2.1.2. Hyperspectral Data Preprocessing

The acquired raw data are L1-A products, and some necessary preprocessing operations, including atmospheric correction, orthorectification correction, bad band removal, and image mosaicking, are required before classification. First, atmospheric correction was performed by Fast Line-of-sight Atmospheric Analysis of Spectral Hypercubes (FLAASH) atmospheric correction using atmospheric parameters obtained from the header file and MODTRAN5 radiative transfer model. Second, atmospheric correction was performed using the Global Digital Elevation Model Version 2 (GDEM 002) (https://search.earthdata.nasa.gov/search/, accessed on 20 September 2021) and rational polynomial coefficient (RPC) models for orthorectification correction. Third, 46 bands affected by UV and water vapor were removed, including 1–3, 63–67, 83–86, 96–107, 122–137, and 161–166. Finally, the acquired multiview images were mosaicked to cover the study area.

2.2. Study Area

The study area is located in Xilinhot Grassland, Xilinhot city, Inner Mongolia Autonomous Region, China, with geographic coordinates between 115°16′37.98″–116°52′32.21″E and 43°18′52.78″–44°29′48.53″N, as shown in Figure 1. A total of four ZY1-02D HSIs were selected, and two views were acquired, with one on 21 May 2021, and one on 13 August 2021, all with cloudiness below 10%. The study area is located in the middle of the Inner Mongolia Plateau, with high topography in the south and low topography in the north, i.e., low hills in the south and gentle undulating plains in the north. The average elevation is 988.5 m, which is a typical temperate semiarid continental climate with an average annual temperature of 1.3–4.8 °C and annual precipitation of 150–400 mm [45,46]. The study area is the main area of Xilin Gol National Nature Reserve and is rich in flora and fauna, with a complete range of grassland types, including typical grasslands with dominant species such as *Stipa grandis* P.A. Smirn., arid grasslands with dominant species such as *Cleistogenes squarrosa* (Trin.) Keng, and meadow grasslands with dominant species such as *Stipa krylovii roshev* and *Achnatherum splendens* (Trin.) Nevski. Thus, the region constitutes a complete ecological series of meadow grasslands-typical grasslands-arid grasslands (ecological variants of typical grasslands) in the Xilin River basin, providing an ideal experimental site for the study and dynamic monitoring of grassland communities in temperate eastern Asia [45].

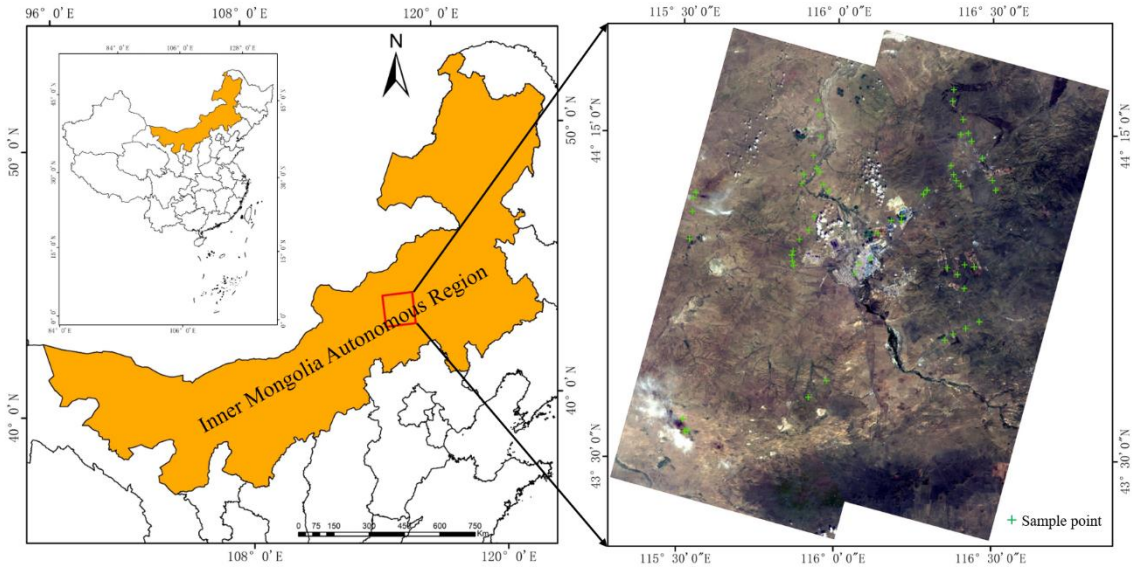

Figure 1. Location of the study area.

2.3. Auxiliary Data

2.3.1. Field Survey Data

A field vegetation survey was conducted in July and August 2021, as shown in Figure 2a. The survey area was mainly the study area covered by the images. The survey was conducted by first circling a 30 m × 30 m area, the size of which was the same as the spatial resolution of ZY1-02D; then, five 1 m × 1 m cells were randomly arranged in the area, and the dominant species in the cells and the corresponding spectral information were obtained, as shown in Figure 2b. A total of 125 sampling points were obtained in the study area, and the distribution of field survey data is shown in the green cross in Figure 1.

2.3.2. Updated Vegetation Map of China (1:1,000,000)

The collection of China's last national vegetation map data began in the 1980s and took 20 years to complete; however, its vegetation distribution has changed dramatically due to climate change and human activities [47]. Therefore, the vegetation map of China urgently needs to be updated to improve our understanding and management of terrestrial ecosystems in China. This vegetation map update utilized "crowdsourcing-change detection classification-expert knowledge", which can better reflect the current vegetation distribution in China and help vegetation management, vegetation restoration, and biodiversity conservation [48].

2.3.3. Functional Zoning Data of the Nature Reserves

The data included the natural concentrated distribution area of representative natural ecosystems and information on rare and endangered wildlife species, including the core area, buffer area, and experimental area [49]. The core area is the core area of ecosystem protection, into which no unit or individual can enter, and scientific research activities are not allowed permitted. The buffer area of a certain area can be designated on the periphery of the core area, and in this area only scientific research and observation activities are permitted. The periphery of the buffer area is designated as the experimental area, and scientific experiments, teaching practice, visits, tourism, and activities such as breeding rare and endangered wildlife are permitted [50].

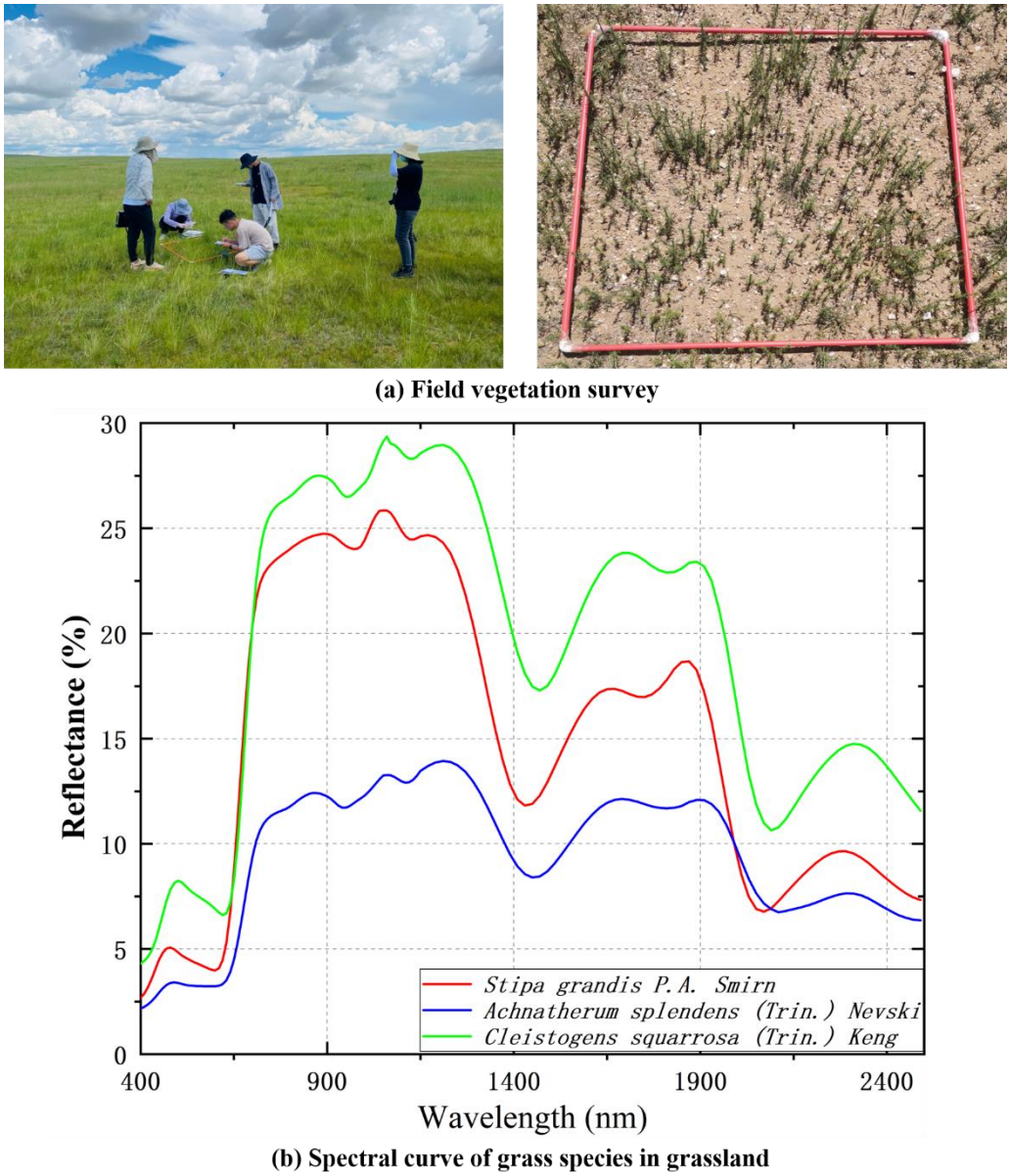

Figure 2. (**a**) Field vegetation survey. (**b**) Spectral curve of grass species in grassland.

3. Methods

3.1. Overview

In this section, we propose an SCM for hyperspectral grassland communities. Figure 3 illustrates the flow chart of the proposed method, which consists of four main parts. The first part was sample acquisition, which included field-collected samples, vegetation map data, and function zoning data. Some pixels within the study area were selected as sample label data, and the correct selection of sample labels directly led to the accuracy of the final grassland community classification. Second, preclassification processing using EMPs to obtain HSIs rich in spatial feature information is capable of distinguishing structural objects or substances. Following classification, the spatial features of grassland communities and the sample label data were input into the RF classifier for training, and the trained model was used to test the images to obtain the preclassification results of the grassland communities. Finally, postclassification processing was conducted, because RF is based on pixel features for classification. This method generates salt-and-pepper noise, which leads to inaccurate grassland classification, so the preclassification results were processed using the LSPF and were input into the RF classifier to obtain the final classification results.

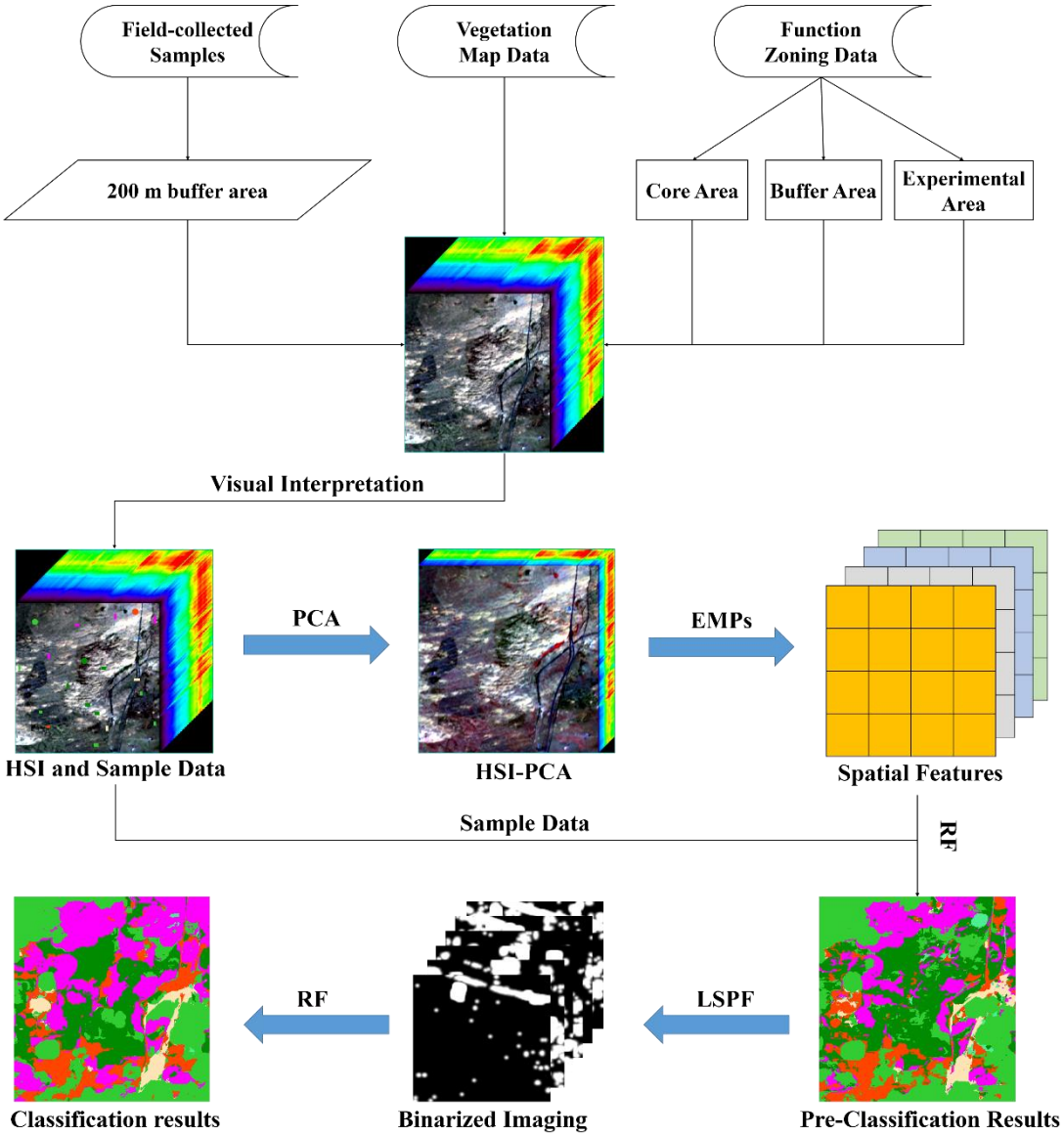

Figure 3. The flowchart of our method.

3.2. Sample Label Data Acquisition

The selection of sample label data determines the accuracy of grassland community delineation to a certain extent. Therefore, to ensure the reasonableness of sample selection, this study combined the field-collected samples, vegetation map data, function zoning data, and ZY1-02D hyperspectral data to construct the sample label data.

Field surveys were conducted in July and August when the grassland vegetation was growing abundantly, and the latitude and longitude coordinates of the survey points and the dominant vegetation type of the grassland were recorded. Then, four ZY1-02D hyperspectral images of Xilinhot, Inner Mongolia Autonomous Region, with a cloudiness of less than 10% and an imaging time in July and August, were selected. Through field investigation, it was found that in a certain area near the 30 m × 30 m sample plot, the vegetation type was basically the same as that of the sample plot. Therefore, a buffer area of 200 m was formed around the actual survey points, and the pixels in the buffer zone were used as sample label data.

The vegetation map data for 2020 are available to the public and contain the geospatial distribution of more than 800 group systems and subgroup systems of 12 vegetation type groups, 55 vegetation types, and approximately 2000 dominant species of communities

in China. Vegetation map data, function zoning data, and image data were overlaid in ArcGIS, and the communities within the core and buffer zones were considered unchanged over the years; however, the communities within the experimental area required sample label selection in conjunction with the current imagery. Through the above process, a total of 13 grassland community types were selected, and details of the sample data are shown in Table 2.

Table 2. The sample information of the Xilinhot grasslands.

Class	Ground Object	Training	Testing
1	*Stipa grandis* P.A. Smirn. (stg)	980	8824
2	*Leymus chinensis* (clg)	63	563
3	*Stipa krylovii roshev* (skr)	41	373
4	*Achnatherum splendens* (Trin.) Nevski (acs)	372	3348
5	Pioneer plant (pip)	7	64
6	Swampy meadow (swm)	20	182
7	*Artemisia desertorum* Spreng. (ard)	122	1094
8	*Caragana liouana* (cal)	143	1287
9	Ulmus pumila (ulp)	34	302
10	*Cleistogenes squarrosa* (Trin.) Keng (cls)	19	167
11	Broadleaved herb (brh)	86	769
12	Crop	8	76
13	Building (bui)	53	481
	Total	1948	17,530

3.3. Extracting Spatial Features of the Xilinhot Grassland Using EMPs

The original HSI data are $X \in \mathbb{R}^{m \times n \times d}$, where $m \times n$ and d are the spatial size and the number of bands, respectively. The HSI consists of d bands, which carry information useful for grassland community classification but often cause information redundancy and an increase in computational effort. Therefore, to reduce the computational effort and spectral dimension, principal component analysis (PCA) [51] was used to process the HSI data from the d-dimension to the p-dimension and to maintain the spatial dimension. Thus, the dimensionality-reduced HSI data are represented as $X_{pca} \in \mathbb{R}^{m \times n \times p}$, where p is the spectral band after PCA.

The spatial features are extracted for X_{pca} using EMP, which mainly includes open and closed transformations. For any pixel x in X_{pca} to perform the first erosion and then expansion open transform, the operation is defined as follows:

$$MP_{\gamma} = \gamma^{k}(x),\ \forall k \in [0, l] \tag{1}$$

where MP_{γ} denotes the image after open transformation; $\gamma^{k}(x)$ denotes the open operation performed on image x; and l is the number of open operations. Then, an expansion was performed followed by an erosion closure transformation on pixel x. The operation is defined as follows:

$$MP_{\Phi} = \Phi^{k}(x), \forall k \in [0, v] \tag{2}$$

where MP_{Φ} denotes the closed transformed image; $\Phi^{k}(x)$ denotes the closed operation on image x; v is the number of closed operations; and k in Equations (1) and (2) is the size of the structure element, and when $k = 0$, it means that no operation is performed on the original image.

Based on the morphological features after the "open transform" and "closed transform", the morphological profile was constructed by selecting the corresponding spectral band, and the morphological profile of pixel x was $p \times (2l + 1)$, i.e., $y^{spa} = \mathrm{EMP}$:

$$\mathrm{EMP} = \{MP_{\gamma}, x, MP_{\Phi}\} \tag{3}$$

The EMP feature extraction method can be used to obtain rich spatial information and to distinguish between structural objects or substances.

3.4. Classification Postprocessing Using LSPF

The spatial features y^{spa} and sample label data obtained from preclassification processing were input to the RF classifier for training, and the preclassification results of grassland communities were obtained by testing the images using the model obtained from the training. Since RF is based on pixel features for classification, it generates salt-and-pepper noise, which leads to inaccurate grassland classification, so it was necessary to perform a postclassification processing operation on the preclassification results. The classification results were further postclassified using the LSPF method to estimate the label probabilities of all pixels in all categories using the spatial correlation with surrounding pixels, and then the probability data and sample label data were input into the classifier to refine the preobtained classification maps and reduce the effect of salt-and-pepper noise on the classification results.

First, the initial classification result map was converted into a series of binary label maps according to whether the pixel belonged to category c. If it belonged to the category, it was set to 1; otherwise, it was 0. For example, if there were 10 categories of feature types in the image scene, the preclassification result map was divided into 10 layers of binary label maps. Second, based on the simplicity and validity of the two-dimensional Gaussian distribution in the real world, the label similarity probability (LSP) was modeled in a local spatial window using the exponential function:

$$g(a,b) = e^{-(a^2+b^2)/2\sigma^2} \tag{4}$$

where $g(a,b)$ is the LSP between the center pixel (value 1) and its neighboring pixels in the same spatial window, e is the natural constant, and σ is the standard deviation.

Further within each spatial window, the LSPF for each class c can be expressed as follows:

$$f_c(i,j) = \sum \boldsymbol{I}_{ij}^c \odot \boldsymbol{G}_{ij} \tag{5}$$

where $f_c(i,j)$ is the cumulative probability of the central pixel (i,j) category c, $\odot$ is the Hadamard product, $\boldsymbol{G}_{ij} = [g(a,b)]$ is the LSP matrix in the $(i,j)\_th$ space window, and $\boldsymbol{I}_{ij}^c = [I^c(a,b)]$ is the Boolean matrix in the preclassified result graph.

Finally, all classes were traversed, and the cumulative probability data of all pixels were obtained as $F_c(i,j) = [f_c(i,j)]_{c=1}^{C}$, which can be expressed as a $1 \times C$ vector. Then, the cumulative probability and sample label data of all pixels were input to the RF classifier, and the trained model was used to test $F_c(i,j)$ to obtain the classification map of the hyperspectral data of the grassland community.

4. Experimental Results and Discussion

4.1. Experimental Setup

In this paper, all experiments were run on a Windows 10 computer with an Intel Core i7-10700 Processor (2.9 GHz), 128 GB of RAM, and an NVIDIA GeForce RTX 3080 Tigraphics card (10 GB of RAM). The training samples of each class were selected randomly based on the number of samples, the percentage of training samples was set to 10, and the remaining samples were used for testing. The EMP parameters were mainly the structural element (SE) and the size of the structural element (k). Referring to the literature [52,53], the SE of the EMP was uniformly chosen as 'disk', and the size of the SE was a series of increasing parameters set as k = [1,3,5,7,9]. In addition, to avoid errors, each method was repeated five times. The overall classification accuracy (OCA), average classification accuracy (ACA), kappa coefficient (KC), and training time t were used in the experiments to evaluate the classification performance of the method.

4.2. Classification Accuracy and Mapping Results

In this section, to verify the effectiveness of the proposed method, seven methods were used for comparison. The traditional classification methods include RF and SVM, where the parameter tree of RF was set to 400, and SVM used the radial basis function (RBF) kernel function. RF-LSPF is the RF classification of the original HSI and LSPF classification postprocessing, and EMP-RF is the result of extracting EMP features from HSI data and is based on RF classification. Deep learning methods include neural networks (NN), 3D fully convolutional networks (3D-FCN) [54], and 3D convolutional neural networks (3D-CNN) [55]. NN is trained with three fully connected layers and classified, 3D-FCN applies multiple 3D local convolution filters of different sizes to jointly utilize the spatial-spectral features of HSIs for classification, and 3D-CNN can extract deep spectral-spatial combined features from HSI data without relying on any preprocessing or postprocessing.

Table 3 shows that the SCM method in this paper achieved the best results in terms of classification accuracy. Its OCA reached 94.56%, which was 26.93% and 15.90% better than that of SVM and RF, respectively. The KC also achieved the highest accuracy of 92.03%, which was 37.38%, 47.67%, and 31.82% better than that of the deep learning methods NN, 3D-FCN, and 3D-CNN, respectively, due to the existence of spatial heterogeneity in the grassland causing the deep learning methods to perform poorly. The OCA of RF-LSPF was improved by 7.00% compared with that of RF, which indicated that postclassification processing was a very necessary step, as seen from the comparison of the SCM and EMP-RF methods. The KC of EMP-RF was improved by 21.51% compared with that of RF, which indicated that preclassification processing had a great contribution to the classification and could even surpass the postclassification processing operation. In this paper, the SCM method obtained the highest classification accuracy in all 12 grassland feature types, among which *Stipa grandis* P.A. Smirn., *Artemisia desertorum* Spreng., *Caragana liouana,* and *Broadleaved herbs* had an accuracy of more than 95%, which well reflects the distribution range of various grassland communities, while other methods were more prone to misclassification. In terms of training time, the SCM time was more moderate and lower than that of the deep learning methods, thus meeting the needs of business-oriented production.

Table 3. Classification accuracy (%) of different methods for the Xilinhot Grassland.

Class	SVM	RF	NN	3D-FCN	3D-CNN	RF-LSPF	EMP-RF	SCM
stg	77.43	93.46	80.42	75.74	82.56	93.30	98.69	**99.12**
clg	6.80	15.10	1.00	2.09	6.23	36.31	34.99	**54.53**
skr	16.63	39.20	52.61	40.39	46.29	54.96	81.77	**88.47**
acs	34.24	64.02	57.13	39.97	59.07	81.05	90.71	**92.59**
pip	14.29	31.88	0	0	27.08	37.81	50.00	**64.06**
swm	43.35	63.96	53.84	41.65	59.45	72.20	75.82	**87.36**
ard	83.91	88.28	80.04	76.65	83.08	93.20	95.80	**97.44**
cal	80.08	81.94	75.55	68.47	83.21	89.26	97.44	**97.75**
ulp	14.53	26.09	24.51	13.85	34.08	54.90	62.58	**72.85**
cls	0	18.68	6.01	7.79	7.58	45.75	51.50	**69.46**
brh	3.10	67.44	24.63	23.65	56.95	83.38	94.02	**95.71**
crop	0	19.21	0	0	0	37.37	**57.89**	43.42
bul	80.92	76.38	77.45	66.28	83.28	88.27	93.35	**96.67**
ACA	35.02	52.74	41.01	35.12	48.37	66.75	75.73	**81.49**
KC	45.11	67.35	54.65	44.36	60.21	78.88	88.86	**92.03**

Table 3. *Cont.*

Class	SVM	RF	NN	3D-FCN	3D-CNN	RF-LSPF	EMP-RF	SCM
OCA	67.63	78.66	71.47	64.71	74.31	85.66	92.47	**94.56**
Train_time(/s)	15.02	**11.20**	254.26	548.39	512.05	106.78	107.69	200.81

Furthermore, the mapping results of the Xilinhot grassland communities obtained by different methods is shown in Figure 4. The distribution range of each community is easily seen. *Stipa grandis* P.A. Smirn. and *Achnatherum splendens* (Trin.) Nevski occupied the main distribution area, and these are the main forage areas in the grassland. Degraded species such as *Caragana liouana* were mainly distributed in the southwestern part of Xilinhot, which is the key area for grassland degradation management. Through the above analysis, the SCM method proposed in this paper can be well applied to large-scale grassland community identification and can provide technical support for decision-makers.

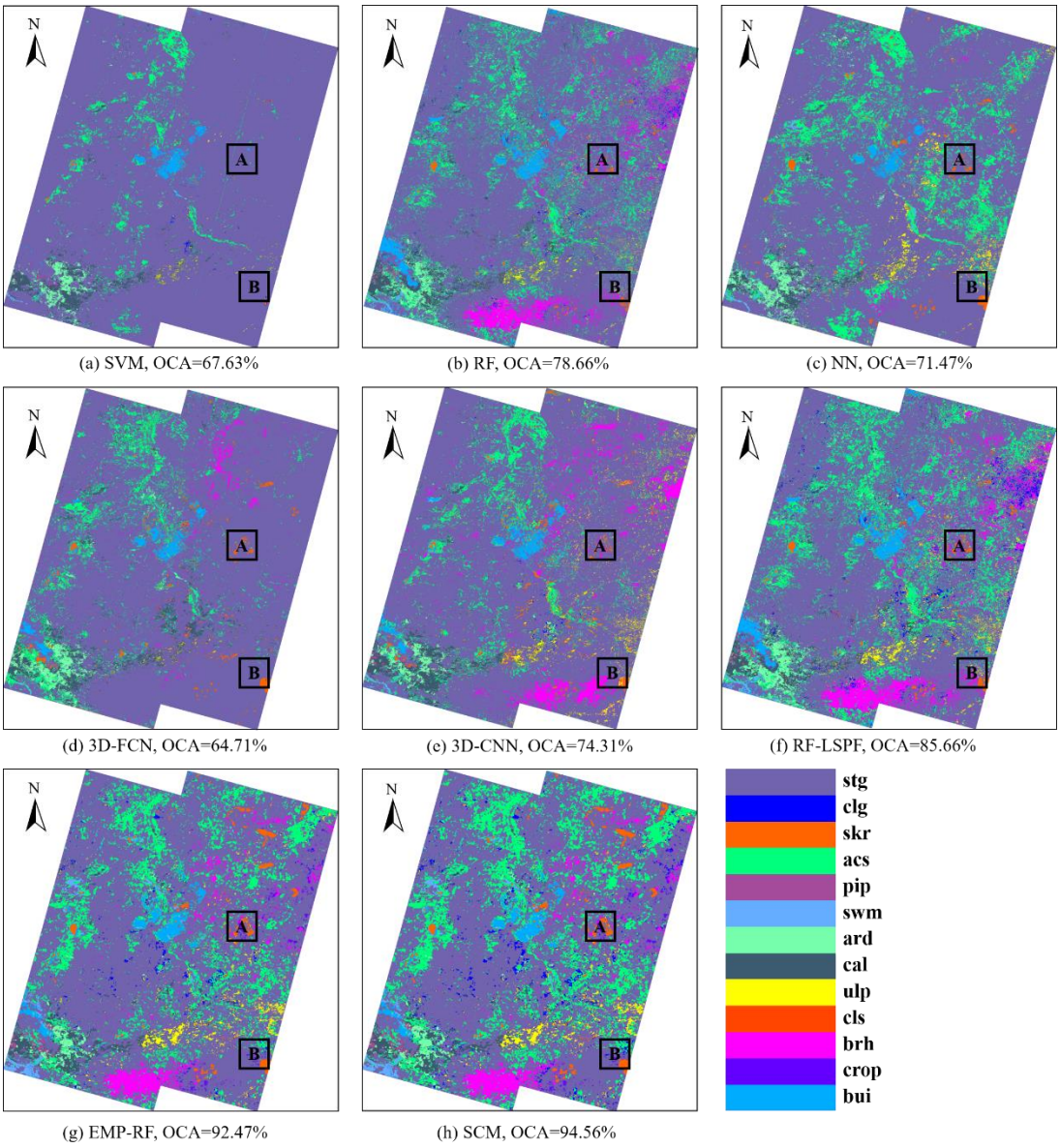

Figure 4. Classification maps obtained using different methods for the Xilinhot Grassland with the corresponding OCA. (**a**–**h**) represent the classification results of SVM, RF, NN, 3D-FCN, 3D-CNN, RF-LSPF, EMP-RF, SCM methods, respectively. Areas A and B will be described in detail in Section 4.3.

4.3. Typical Area Analysis

Compared with UAV remote sensing and ground remote sensing, satellite remote sensing has the ability of large-scale observation [56,57]. The grassland community vegetation has the characteristics of wide distribution and large cross-regional distribution. Therefore, the application of satellite remote sensing has greater application potential. In this study, satellite hyperspectral remote sensing was used to classify and map grassland communities in Xilinhot Grassland. In order to express the distribution pattern of grassland communities in more detail, areas A and B in Figure 4 were analyzed separately.

Area A in Figure 5 is located directly east of Xilinhot City, its main grassland community type is *Stipa grandis* P.A. Smirn., and the rest of the dominant species are *Stipa krylovii roshev*, *Achnatherum splendens* (Trin.) Nevski, crop, etc. *Stipa grandis* P.A. Smirn. is a perennial dense clump herb that grows in temperate and semi-arid climate zones. Its basal leaves are abundant and can be preserved relatively intact until winter and spring, which can provide a large amount of forage for livestock. Figure 6(a1,a2) are field investigation photos of *Stipa grandis* P.A. Smirn., and (b1) and (b2) are field investigation photos of *Achnatherum splendens* (Trin.) Nevski. The SCM proposed in this paper can clearly map the distribution range of land object types such as *Stipa grandis* P.A. Smirn. Combined with Table 3, it is obvious that both preclassification and postclassification processing can be of great help for improving the mapping results.

Area B in Figure 7 is located in the southeast of Xilinhot City. Similar to Area A, *Stipa grandis* P.A. Smirn. is also dominant. Compared with the SVM, RF, NN, and 3D-FCN methods, SCM can map the distribution range of various grassland communities in more detail, which also proves that preclassification processing can improve the model training ability. Compared with the EMP-RF method, the LSPF method can reduce the influence of salt-and-pepper noise on the mapping results, indicating that postclassification processing can further improve the classification accuracy.

4.4. Disadvantages of Hyperspectral Images

HSIs show considerable potential in data mining, but great problems also exist.

(1) Given a limited number of training samples, when the feature dimension increases to a certain number, the classification accuracy may decrease as the feature dimension increases: a phenomenon known as the "Hughes" phenomenon. This phenomenon renders the HSIs unable to accurately identify the target properties, and satisfactory results are difficult to obtain. Two reasons exist for this phenomenon: (1) ground truth label samples with sufficient and representative distribution in the statistical sense are very difficult to obtain; (2) the training data and the test data are usually assumed to obey the same data distribution, but the ground object scene is complex, and the real distribution of the data space is difficult to accurately describe with a limited number of training samples.

(2) The atlas integration of HSIs provides strong support for the joint analysis of multisource features, but some difficulties also exist in the fusion of multisource information: (1) if texture features and spectral features are used simultaneously, the resulting feature space will be larger, and the "Hughes" phenomenon will be more prominent; (2) when spatial information is introduced, more prior knowledge needs to be introduced to be able to more accurately interpret the target, such as information on the shape and neighbor correlation.

(3) The heterogeneity of the material itself, image resolution, mixed pixels, noise, and other factors may lead to changes in the spectrum, and such changes may cause two adverse effects: (1) the spectrum of similar ground objects has changed, including the difference in spectral amplitude and spectral angle, which can easily lead to omissions and errors in the interpretation process; (2) after the spectra of different targets are perturbed, the originally inconspicuous spectral differences are submerged.

(4) Usually, remote sensing images, especially HSIs, have a large amount of data. The large amount of data occupied by hundreds or thousands of spectral images increases the resource consumption of computing and storage and reduces the efficiency of HSI interpretation.

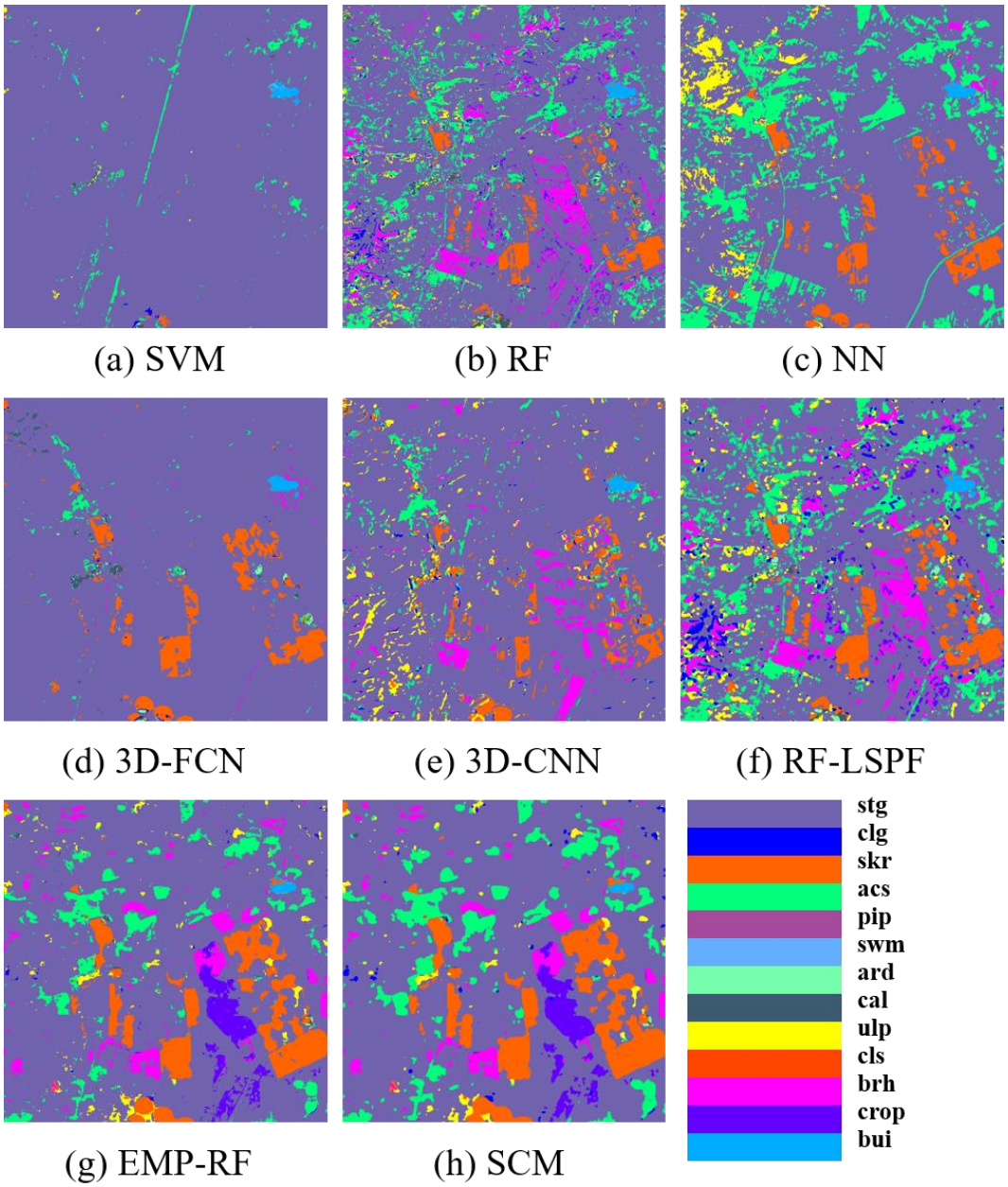

Figure 5. Typical taxonomic region A of grassland communities in Xilinhot. (**a**–**h**) represent the classification results of SVM, RF, NN, 3D-FCN, 3D-CNN, RF-LSPF, EMP-RF, SCM methods, respectively.

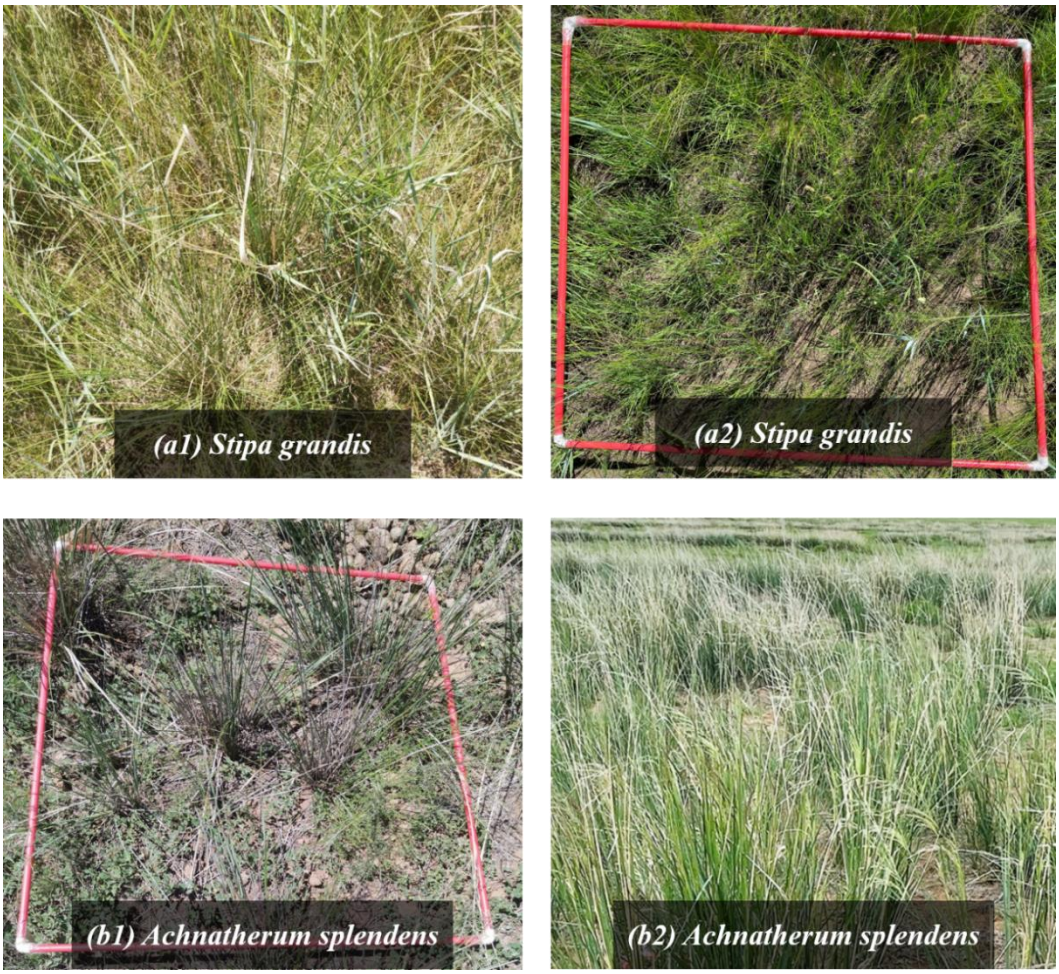

Figure 6. Photos for (**a1**,**a2**) *Stipa grandis* P.A. Smirn. and (**b1**,**b2**) *Achnatherum splendens* from the filed investigation in 2021.

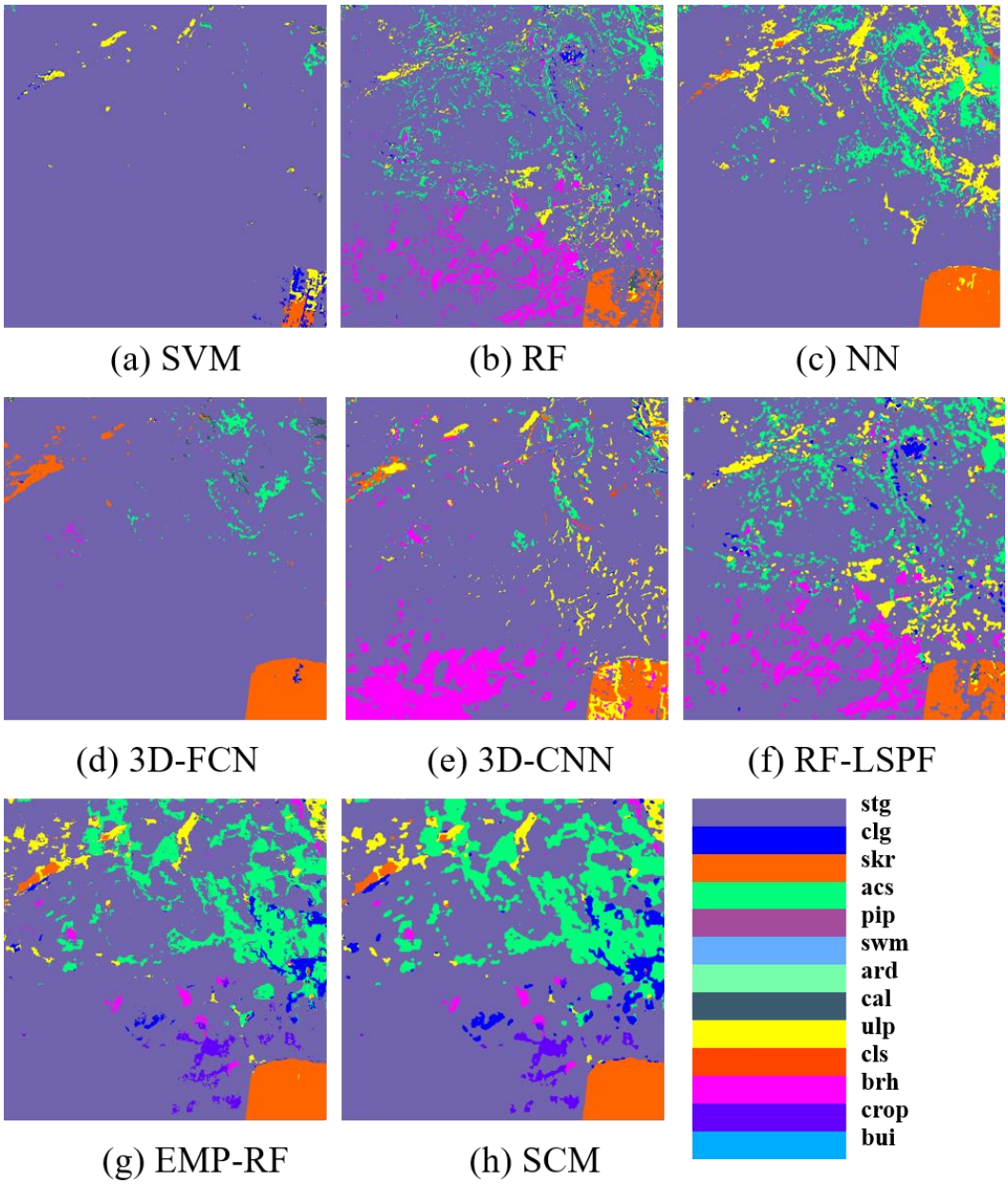

Figure 7. Typical taxonomic region B of grassland communities in Xilinhot. (**a**–**h**) represent the classification results of SVM, RF, NN, 3D-FCN, 3D-CNN, RF-LSPF, EMP-RF, SCM methods, respectively.

5. Conclusions

In this paper, we explored the distribution pattern of grassland communities in Xilinhot using China ZY1-02D HSI satellite data and proposed a systematic hyperspectral grassland community classification method for this purpose. The method includes sample label data acquisition, preclassification processing, classification model training, and postclassification processing, and the importance of preclassification processing and postclassification processing on the results was verified through experiments. Compared with the seven methods, SCM had the highest classification accuracy (with OCA = 94.56%), a more moderate computation time (with train_time = 200.81 s), and a greater advantage in mapping. In addition, we analyzed typical community distributions, which will help decision-makers develop appropriate responses to specific needs. In the future, we will consider a combination of hyperspectral and high spatial resolution data for grassland community identification to further improve the classification performance.

Author Contributions: Conceptualization, D.W. and K.L.; methodology, D.W.; software, W.S.; validation, C.X., W.L. and L.L.; formal analysis, X.H.; investigation, C.F.; resources, C.X.; data curation, D.W.; writing—original draft preparation, K.L.; writing—review and editing, D.W.; visualization, W.L.; supervision, W.S.; project administration, D.W.; funding acquisition, D.W. All authors have read and agreed to the published version of the manuscript.

Funding: This research was funded by National Natural Science Foundation of China, grant number 42101412.

Data Availability Statement: All ZY1-02D hyperspectral data used in this analysis can be accessed with the Natural Resources Satellite Remote Sensing Cloud Service Platform (http://sasclouds.com/chinese/home, accessed on 5 September 2021).

Conflicts of Interest: The authors declare no conflict of interest.

References

1. Zhou, W.; Gang, C.; Zhou, L.; Chen, Y.; Li, J.; Ju, W.; Odeh, I. Dynamic of grassland vegetation degradation and its quantitative assessment in the northwest China. *Acta Oecologica* **2014**, *55*, 86–96. [CrossRef]
2. Liu, Y.; Wang, Q.; Zhang, Z.; Tong, L.; Wang, Z.; Li, J. Grassland dynamics in responses to climate variation and human activities in China from 2000 to 2013. *Sci. Total Environ.* **2019**, *690*, 27–39. [CrossRef] [PubMed]
3. Chen, Y.; Mu, S.; Sun, Z.; Gang, C.; Li, J.; Padarian, J.; Groisman, P.; Chen, J.; Li, S. Grassland carbon sequestration ability in China: A new perspective from terrestrial aridity zones. *Rangel. Ecol. Manag.* **2016**, *69*, 84–94. [CrossRef]
4. Emberson, L. Effects of ozone on agriculture, forests and grasslands. *Philos. Trans. R. Soc. A* **2020**, *378*, 20190327. [CrossRef]
5. Zhou, W.; Yang, H.; Huang, L.; Chen, C.; Lin, X.; Hu, Z.; Li, J. Grassland degradation remote sensing monitoring and driving factors quantitative assessment in China from 1982 to 2010. *Ecol. Indic.* **2017**, *83*, 303–313. [CrossRef]
6. He, C.; Tian, J.; Gao, B.; Zhao, Y. Differentiating climate-and human-induced drivers of grassland degradation in the Liao River Basin, China. *Environ. Monit. Assess.* **2015**, *187*, 4199. [CrossRef]
7. Zhang, R.; Liang, T.; Guo, J.; Xie, H.; Feng, Q.; Aimaiti, Y. Grassland dynamics in response to climate change and human activities in Xinjiang from 2000 to 2014. *Sci. Rep.* **2018**, *8*, 2888. [CrossRef]
8. Han, Z.; Song, W.; Deng, X.; Xu, X. Grassland ecosystem responses to climate change and human activities within the Three-River Headwaters region of China. *Sci. Rep.* **2018**, *8*, 9079. [CrossRef]
9. Yu, C.; Zhang, Y.; Claus, H.; Zeng, R.; Zhang, X.; Wang, J. Ecological and environmental issues faced by a developing Tibet. *ACS Publ.* **2012**, *46*, 1979–1980. [CrossRef]
10. Wu, J.; Mao, R.; Li, M.; Xia, J.; Song, J.; Cheng, D.; Sun, H. Assessment of aquatic ecological health based on determination of biological community variability of fish and macroinvertebrates in the Weihe River Basin, China. *J. Environ. Manag.* **2020**, *267*, 110651. [CrossRef]
11. Jackson, R.B.; Canadell, J.; Ehleringer, J.R.; Mooney, H.; Sala, O.; Schulze, E.-D. A global analysis of root distributions for terrestrial biomes. *Oecologia* **1996**, *108*, 389–411. [CrossRef]
12. Woodward, F.I.; Lomas, M.R.; Kelly, C.K. Global climate and the distribution of plant biomes. *Philos. Trans. R. Soc. Lond. Ser. B Biol. Sci.* **2004**, *359*, 1465–1476. [CrossRef]
13. Mansour, K.; Mutanga, O.; Everson, T.; Adam, E. Discriminating indicator grass species for rangeland degradation assessment using hyperspectral data resampled to AISA Eagle resolution. *ISPRS J. Photogramm. Remote Sens.* **2012**, *70*, 56–65. [CrossRef]
14. Li, B. Rangeland degradation in northern China and strategies for its prevention. *Sci. Agric. Sin.* **1997**, *30*, 1–8.
15. Quangong, C. Current status and development of grassland monitoring in China. *Pratacult. Sci.* **2008**, *25*, 29–38.
16. Cardellach, E.; Padullés, R.; Tomás, S.; Turk, F.; Ao, C.; de la Torre-Juárez, M. Probability of intense precipitation from polarimetric GNSS radio occultation observations. *Q. J. R. Meteorol. Soc.* **2018**, *144*, 206–220. [CrossRef]
17. Song, D.; Zhen, Z.; Wang, B.; Li, X.; Gao, L.; Wang, N.; Xie, T.; Zhang, T. A novel marine oil spillage identification scheme based on convolution neural network feature extraction from fully polarimetric SAR imagery. *IEEE Access* **2020**, *8*, 59801–59820. [CrossRef]
18. Toté, C.; Patricio, D.; Boogaard, H.; Van der Wijngaart, R.; Tarnavsky, E.; Funk, C. Evaluation of satellite rainfall estimates for drought and flood monitoring in Mozambique. *Remote Sens.* **2015**, *7*, 1758–1776. [CrossRef]
19. Tian, H.; Wu, M.; Wang, L.; Niu, Z. Mapping early, middle and late rice extent using sentinel-1A and Landsat-8 data in the poyang lake plain, China. *Sensors* **2018**, *18*, 185. [CrossRef]
20. Balogun, A.-L.; Yekeen, S.T.; Pradhan, B.; Althuwaynee, O.F. Spatio-temporal analysis of oil spill impact and recovery pattern of coastal vegetation and wetland using multispectral satellite landsat 8-OLI imagery and machine learning models. *Remote Sens.* **2020**, *12*, 1225. [CrossRef]
21. Wang, X.; Gao, X.; Zhang, Y.; Fei, X.; Chen, Z.; Wang, J.; Zhang, Y.; Lu, X.; Zhao, H. Land-cover classification of coastal wetlands using the RF algorithm for Worldview-2 and Landsat 8 images. *Remote Sens.* **2019**, *11*, 1927. [CrossRef]
22. Su, H.; Yao, W.; Wu, Z.; Zheng, P.; Du, Q. Kernel low-rank representation with elastic net for China coastal wetland land cover classification using GF-5 hyperspectral imagery. *ISPRS J. Photogramm. Remote Sens.* **2021**, *171*, 238–252. [CrossRef]

23. San Martín, L.; Morandeira, N.S.; Grimson, R.; Rajngewerc, M.; González, E.B.; Kandus, P. The contribution of ALOS/PALSAR-1 multi-temporal data to map permanently and temporarily flooded coastal wetlands. *Int. J. Remote Sens.* **2020**, *41*, 1582–1602. [CrossRef]
24. Shen, X.; Wang, D.; Mao, K.; Anagnostou, E.; Hong, Y. Inundation extent mapping by synthetic aperture radar: A review. *Remote Sens.* **2019**, *11*, 879. [CrossRef]
25. Ishida, T.; Kurihara, J.; Viray, F.A.; Namuco, S.B.; Paringit, E.C.; Perez, G.J.; Takahashi, Y.; Marciano, J.J., Jr. A novel approach for vegetation classification using UAV-based hyperspectral imaging. *Comput. Electron. Agric.* **2018**, *144*, 80–85. [CrossRef]
26. Audebert, N.; Le Saux, B.; Lefèvre, S. Deep learning for classification of hyperspectral data: A comparative review. *IEEE Geosci. Remote Sens. Mag.* **2019**, *7*, 159–173. [CrossRef]
27. Hestir, E.L.; Brando, V.E.; Bresciani, M.; Giardino, C.; Matta, E.; Villa, P.; Dekker, A.G. Measuring freshwater aquatic ecosystems: The need for a hyperspectral global mapping satellite mission. *Remote Sens. Environ.* **2015**, *167*, 181–195. [CrossRef]
28. Sun, W.; Liu, K.; Ren, G.; Liu, W.; Yang, G.; Meng, X.; Peng, J. A simple and effective spectral-spatial method for mapping large-scale coastal wetlands using China ZY1-02D satellite hyperspectral images. *Int. J. Appl. Earth Obs. Geoinf.* **2021**, *104*, 102572. [CrossRef]
29. Carrizosa, E.; Morales, D.R. Supervised classification and mathematical optimization. *Comput. Oper. Res.* **2013**, *40*, 150–165. [CrossRef]
30. Jiao, L.; Sun, W.; Yang, G.; Ren, G.; Liu, Y. A hierarchical classification framework of satellite multispectral/hyperspectral images for mapping coastal wetlands. *Remote Sens.* **2019**, *11*, 2238. [CrossRef]
31. Le Bris, A.; Rosa, P.; Lerouxel, A.; Cognie, B.; Gernez, P.; Launeau, P.; Robin, M.; Barillé, L. Hyperspectral remote sensing of wild oyster reefs. *Estuar. Coast. Shelf Sci.* **2016**, *172*, 1–12. [CrossRef]
32. Camps-Valls, G.; Gomez-Chova, L.; Munoz-Mari, J.; Vila-Frances, J.; Calpe-Maravilla, J. Composite kernels for hyperspectral image classification. *IEEE Geosci. Remote Sens. Lett.* **2006**, *3*, 93–97. [CrossRef]
33. Li, W.; Du, Q. Joint Within-Class Collaborative Representation for Hyperspectral Image Classification. *IEEE J. Sel. Top. Appl. Earth Obs. Remote Sens.* **2014**, *7*, 2200–2208. [CrossRef]
34. Gao, Q.; Lim, S.; Jia, X. Spectral–spatial hyperspectral image classification using a multiscale conservative smoothing scheme and adaptive sparse representation. *IEEE Trans. Geosci. Remote Sens.* **2019**, *57*, 7718–7730. [CrossRef]
35. Cao, X.; Xu, Z.; Meng, D. Spectral-Spatial Hyperspectral Image Classification via Robust Low-Rank Feature Extraction and Markov Random Field. *Remote Sens.* **2019**, *11*, 1565. [CrossRef]
36. Kang, X.; Li, S.; Benediktsson, J.A. Spectral–spatial hyperspectral image classification with edge-preserving filtering. *IEEE Trans. Geosci. Remote Sens.* **2013**, *52*, 2666–2677. [CrossRef]
37. Song, W.; Li, S.; Fang, L.; Lu, T. Hyperspectral image classification with deep feature fusion network. *IEEE Trans. Geosci. Remote Sens.* **2018**, *56*, 3173–3184. [CrossRef]
38. Xu, Y.; Du, B.; Zhang, L. Beyond the patchwise classification: Spectral-spatial fully convolutional networks for hyperspectral image classification. *IEEE Trans. Big Data* **2019**, *6*, 492–506. [CrossRef]
39. Roy, S.K.; Manna, S.; Song, T.; Bruzzone, L. Attention-based adaptive spectral–spatial kernel ResNet for hyperspectral image classification. *IEEE Trans. Geosci. Remote Sens.* **2020**, *59*, 7831–7843. [CrossRef]
40. Paoletti, M.; Haut, J.; Plaza, J.; Plaza, A. A new deep convolutional neural network for fast hyperspectral image classification. *ISPRS J. Photogramm. Remote Sens.* **2018**, *145*, 120–147. [CrossRef]
41. Asghari Beirami, B.; Mokhtarzade, M. Spatial-Spectral Classification of Hyperspectral Images Based on Extended Morphological Profiles and Guided Filter. *Comput. Knowl. Eng.* **2020**, *2*, 2–8.
42. Yu, J.; Liang, D.; Han, B.; Gao, H. Study on ground object classification based on the hyperspectral fusion images of ZY-1 (02D) satellite. *J. Appl. Remote Sens.* **2021**, *15*, 042603. [CrossRef]
43. Lu, H.; Qiao, D.; Li, Y.; Wu, S.; Deng, L. Fusion of China ZY-1 02D Hyperspectral Data and Multispectral Data: Which Methods Should Be Used? *Remote Sens.* **2021**, *13*, 2354. [CrossRef]
44. Xu, Z.; Chen, S.; Zhu, B.; Chen, L.; Ye, Y.; Lu, P. Evaluating the Capability of Satellite Hyperspectral Imager, the ZY1–02D, for Topsoil Nitrogen Content Estimation and Mapping of Farmlands in Black Soil Area, China. *Remote Sens.* **2022**, *14*, 1008. [CrossRef]
45. Lyu, X.; Li, X.; Gong, J.; Wang, H.; Dang, D.; Dou, H.; Li, S.; Liu, S. Comprehensive grassland degradation monitoring by remote sensing in Xilinhot, Inner Mongolia, China. *Sustainability* **2020**, *12*, 3682. [CrossRef]
46. Sun, B.; Li, Z.; Gao, Z.; Guo, Z.; Wang, B.; Hu, X.; Bai, L. Grassland degradation and restoration monitoring and driving forces analysis based on long time-series remote sensing data in Xilin Gol League. *Acta Ecol. Sin.* **2017**, *37*, 219–228. [CrossRef]
47. Zhang, X.; Sun, S.; Yong, S.; Zhou, Z.; Wang, R. Vegetation map of the People's Republic of China (1:1,000,000). *Geol. Publ. House* **2007**.
48. Su, Y.; Guo, Q.; Hu, T.; Guan, H.; Jin, S.; An, S.; Chen, X.; Guo, K.; Hao, Z.; Hu, Y. An updated vegetation map of China (1:1,000,000). *Sci. Bull.* **2020**, *65*, 1125–1136. [CrossRef]
49. Liu, F.; Feng, C.; Zhou, Y.; Zhang, L.; Du, J.; Huang, W.; Luo, J.; Wang, W. Effectiveness of functional zones in National Nature Reserves for the protection of forest ecosystems in China. *J. Environ. Manag.* **2022**, *308*, 114593. [CrossRef]
50. Tang, J.; Lu, H.; Xue, Y.; Li, J.; Li, G.; Mao, Y.; Deng, C.; Li, D. Data-driven planning adjustments of the functional zoning of Houhe National Nature Reserve. *Glob. Ecol. Conserv.* **2021**, *29*, e01708. [CrossRef]

51. Kherif, F.; Latypova, A. Principal Component Analysis. In *Machine Learning*; Elsevier: Amsterdam, The Netherlands, 2020; pp. 209–225.
52. Benediktsson, J.A.; Palmason, J.A.; Sveinsson, J.R. Classification of hyperspectral data from urban areas based on extended morphological profiles. *IEEE Trans. Geosci. Remote Sens.* **2005**, *43*, 480–491. [CrossRef]
53. Huang, X.; Zhang, L. An SVM ensemble approach combining spectral, structural, and semantic features for the classification of high-resolution remotely sensed imagery. *IEEE Trans. Geosci. Remote Sens.* **2012**, *51*, 257–272. [CrossRef]
54. Lee, H.; Kwon, H. Contextual deep CNN based hyperspectral classification. In Proceedings of the 2016 IEEE International Geoscience and Remote Sensing Symposium (IGARSS), Beijing, China, 10–15 July 2016; pp. 3322–3325.
55. Li, Y.; Zhang, H.; Shen, Q. Spectral–spatial classification of hyperspectral imagery with 3D convolutional neural network. *Remote Sens.* **2017**, *9*, 67. [CrossRef]
56. Zhao, R.; Li, Y.; Ma, M. Mapping paddy rice with satellite remote sensing: A review. *Sustainability* **2021**, *13*, 503. [CrossRef]
57. Coffer, M.M.; Schaeffer, B.A.; Salls, W.B.; Urquhart, E.; Loftin, K.A.; Stumpf, R.P.; Werdell, P.J.; Darling, J.A. Satellite remote sensing to assess cyanobacterial bloom frequency across the United States at multiple spatial scales. *Ecol. Indic.* **2021**, *128*, 107822. [CrossRef] [PubMed]